



HAL
open science

Data-driven methods for discovery of next-generation electrostrictive materials

Dennis Trujillo, Ashok Gurung, Jiacheng Yu, Sanjeev Nayak, S. Pamir Alpay, Pierre-Eymeric Janolin

► **To cite this version:**

Dennis Trujillo, Ashok Gurung, Jiacheng Yu, Sanjeev Nayak, S. Pamir Alpay, et al.. Data-driven methods for discovery of next-generation electrostrictive materials. npj Computational Materials, 2022, 8 (1), pp.251. 10.1038/s41524-022-00941-1 . hal-03903429

HAL Id: hal-03903429

<https://centralesupelec.hal.science/hal-03903429>

Submitted on 19 Dec 2022

HAL is a multi-disciplinary open access archive for the deposit and dissemination of scientific research documents, whether they are published or not. The documents may come from teaching and research institutions in France or abroad, or from public or private research centers.

L'archive ouverte pluridisciplinaire **HAL**, est destinée au dépôt et à la diffusion de documents scientifiques de niveau recherche, publiés ou non, émanant des établissements d'enseignement et de recherche français ou étrangers, des laboratoires publics ou privés.

Data-Driven Methods for Discovery of Next-Generation Electrostrictive Materials

Dennis Trujillo,^{a,b} Ashok Gurung,^c Jiacheng Yu,^d Sanjeev K. Nayak,^a S. Pamir Alpay,^{a,c}
and Pierre-Eymeric Janolin^{d,*}

^a*Department of Materials Science and Engineering and Institute of Materials Science,
University of Connecticut, Storrs, CT 06269, USA*

^b*X-Ray Science Division, Argonne National Laboratory, Lemont, IL 60654, USA*

^c*Department of Physics, University of Connecticut, Storrs, CT 06269, USA*

^d*Université Paris-Saclay, CentraleSupélec, CNRS, Laboratoire SPMS, 91190 Gif-sur-Yvette,
France*

**email: pierre-eymeric.janolin@centralesupelec.fr*

Abstract

All dielectrics exhibit electrostriction, *i.e.*, display a quadratic strain response to an electric field compared to the linear strain dependence of piezoelectrics. As such, there is significant interest in discovering new electrostrictors with enhanced electrostrictive coefficients, especially as electrostrictors can exhibit effective piezoelectricity when a bias electric field is applied. We present the results of a study combining data mining and first-principles computations that indicate that there exists a group of iodides, bromides, and chlorides that have electrostrictive coefficients exceeding $10 \text{ m}^4 \text{ C}^{-2}$ which are substantially higher than typical oxide electrostrictive ceramics and polymers. The corresponding effective piezoelectric voltage coefficients are three orders of magnitude larger than lead zirconate titanate.

Keywords: Electrostriction, data mining, first-principles calculation, halides

INTRODUCTION

The development of novel materials exhibiting exceptional strain response in the presence of an external electric field is imperative to the development of tunable electromechanical devices¹⁻⁸. Promising applications involve next-generation transducers⁹, ultra-efficient actuators^{1,2,10}, sonars¹¹, and low power logic devices¹² with application spaces in medicine, astronomy, and consumer electronics. Recent discoveries of ‘giant’ electrostrictors, for example, Gd-doped ceria⁸, and (Nb, Y) doping in bismuth oxide¹³ and lanthanum molybdenum oxide⁷, soft nano-composite based on carbon nanotubes (CNT)¹⁴ and liquid crystalline graphene⁶ have opened promising applications for superior electromechanical properties, and also as a replacement of lead-based $\text{Pb}(\text{Ti}_{1-x}\text{Zr}_x)\text{O}_3$ (PZT) solid solutions that are widely used in current applications. Of particular interest is the possibility to induce an effective piezoelectric behavior under bias electric field, generating extraordinarily large piezoelectric coefficients ($d_{33} \sim 2 \times 10^5 \text{ pC N}^{-1}$)¹⁵. These ‘giant’ electrostrictors have been reviewed recently¹⁶. There is a clear advantage in utilizing electrostrictive materials that exhibit a quadratic strain in response to an electric field. This may allow for a more significant strain response for a given applied external field, as well as take advantage of the anhysteretic nature of electrostriction for high-precision displacements.

This effect is mediated via an applied electric field (E_i) and the dielectric polarization (P_i) vectors as described by:

$$x_{ij} = d_{ijk}E_k + M_{ijkl}E_kE_l \quad (1)$$

$$x_{ij} = g_{ijk}P_k + Q_{ijkl}P_kP_l \quad (2)$$

where x_{ij} are the strain components, d_{ijk} and g_{ijk} are piezoelectric tensors, and M_{ijkl} and Q_{ijkl} are fourth-rank tensors describing the electrostrictive response. In Equation (1), the total strain (at constant stress) is expressed in terms of an applied electric field, whereas in Equation (2) it is given as a function of the polarization. The M tensor is of particular interest for actuator applications whereas Q is used as a design criterion in sensing applications.

The search for novel electrostrictors has historically appeared bounded by the universal empirical relation connecting the electrostrictive coefficient to the ratio of the elastic compressibility over the permittivity⁵ until the discovery of ‘giant’ electrostrictors that are several orders of magnitude greater than the empirically expected values¹⁶. These include materials such as $\text{La}_2\text{Mo}_2\text{O}_9$ ($M_h \sim 10^{-18} \text{ m}^2 \text{ V}^{-2}$ and $Q_h \sim 20 \text{ m}^4 \text{ C}^{-2}$), (Nb,Y)-stabilized Bi_2O_3 ($M_h \sim 4.7 - 12.5 \times 10^{-18} \text{ m}^2 \text{ V}^{-2}$ and $Q_h \sim 83-273 \text{ m}^4 \text{ C}^{-2}$)¹³, CeO_{2-x} ($M_h \sim 300 \times 10^{-18} \text{ m}^2 \text{ V}^{-2}$)¹⁵, lead halide perovskites ($M_h \sim 730 - 900 \times 10^{-18} \text{ m}^2 \text{ V}^{-2}$ and $Q_h \sim 1266 - 1417 \text{ m}^4 \text{ C}^{-2}$)¹⁷, and $\text{Ce}_{0.8}\text{Gd}_{0.2}\text{O}_{1.9}$ ($M_h \sim 6.5 \times 10^{-18} \text{ m}^2 \text{ V}^{-2}$)⁶⁻⁸. The electrostriction coefficients of these materials are three orders larger than typical perovskites, including BaTiO_3 , PbTiO_3 , SrTiO_3 , and $\text{Pb}(\text{Ti}_{1-x}\text{Zr}_x)\text{O}_3$ for which Q_h is in the range $0.02 - 0.07 \text{ m}^4 \text{ C}^{-2}$.

Using large open materials databases composed of accurately determined materials properties, the programmatic search for materials exhibiting specific properties becomes possible. In line with data-driven methods, advanced modeling approaches across length scales, and the successful insertion of the concept of materials genomics that allows for rapid development and deployment of novel materials^{18,19}, we employ here a combination of data mining and first-principles modeling in the discovery of materials exhibiting exceptional electrostrictive coefficients. Our results show several non-oxide inorganic compounds with

electrostrictive properties of one or two orders of magnitude higher than existing oxide ceramics and with comparable or higher electrostriction coefficients of polymers.

RESULTS

Assessment of Electrostrictive Properties

The tensorial notation that has been employed in Equations (1) and (2) can be reduced to the following criteria to assess the magnitude of the electrostrictive properties of a wide variety of materials (see Supplementary Information), which is also defined as the Newnham's proxy Q_h^{proxy} , based on the approach presented in Refs. ^{5,10}. M_h^{proxy} can be derived from Q_h^{proxy} as below:

$$Q_h^{\text{proxy}} = \left(\frac{s_R}{\varepsilon_0 \varepsilon_r} \right) \approx (K_R \varepsilon^*)^{-1} \quad (3)$$

$$M_h^{\text{proxy}} = \frac{\varepsilon^*}{K_R}. \quad (4)$$

Here ε^* is the average eigenvalue of the dielectric tensor ε with $\varepsilon = \varepsilon_0 \varepsilon_r$, ε_r the relative permittivity of the material, and ε_0 the permittivity of vacuum. s_R in Equation (3) is the Reuss elastic compressibility given as ^{20,21}:

$$\frac{1}{K_R} = s_R = (s_{11} + s_{22} + s_{33}) + 2(s_{12} + s_{23} + s_{31}) \quad (5)$$

The Supplementary Information provides a more detailed treatment to define constitutive relations for the electrostrictive coefficients M_{ijkl} and Q_{ijkl} . Equations (3) and (4) follow from specific electrical and mechanical boundary conditions corresponding to hydrostatic pressure/expansion and a single electric field component (uniaxial applied electric field in a

short-circuit configuration) as discussed in the Supplementary Information. We note that Equation (3) describes the Q_h criterion used by Newnham *et al.* in their landmark paper that classified electrostriction for a range of materials over an extensive response space⁵. We add here an additional criterion for M_h ^{16,22}. Although closely related, the quantities M_h and Q_h are not interchangeable as converse effects (Supplementary Information). Subtle differences in how these are defined give rise to slightly different criteria for the proxy derivation used to approximate M_h and Q_h . M_h is readily accessible physical parameter in experiments.

In addition to the static empirical relations in Equation (3) and Equation (4), it is advantageous to use the differential forms of Q_h and M_h as described in the Supplementary Information, which is essentially the dielectric response with change in external hydrostatic pressure (p). In the following, Q_h and M_h derived from our density functional theory (DFT) calculations are defined as Q_h^{DFT} and M_h^{DFT} , respectively. Thus,

$$Q_h^{\text{DFT}} = -0.5 \left(\frac{\partial(1/\varepsilon^*)}{\partial p} \right) \quad (6)$$

$$M_h^{\text{DFT}} = 0.5 \left(\frac{\partial \varepsilon^*}{\partial p} \right) \quad (7)$$

It must be noted that Equations (6) and (7) capture the mechanical response as differential in pressure (p) and the equations are independent of Equation (3) and Equation (4).

DFT has been used to study electrostriction properties of compounds having high structural symmetry^{23,24}. Of particular interest in this regard is the study by Tanner *et al.* wherein the electrostrictive coefficients of cubic dielectric materials were computed using the differentials of the lattice parameters, which is similar to differentials of hydrostatic pressure for cubic crystal system²⁵. We have adopted the latter method using Equation (6) and Equation (7). In our computations, the trace of external stress tensor, defined as $pstress$, is treated as the

hydrostatic pressure with the conventional notation that positive and negative *pstress* values mean hydrostatic expansion and compression, respectively. This approach allows for uniform evaluation of electrostrictive coefficients over all seven crystal systems independent of their crystal structure.

Data Mining

To assign proxies for selecting materials exhibiting high electrostriction, we utilize a set of relationships between the dielectric response, the elastic coefficients, the electric field-induced strain, and the electrostrictive properties of materials as described in the previous section. A similar methodology developed by Newnham *et al.* has shown a semi-empirical connection between the elastic compliance, the dielectric response, and the hydrostatic electrostrictive coefficient Q_h ^{4,5}.

Existing databases of calculated functional properties provide easy access to data that can be used to shortlist materials with exceptional properties via a simple database query of related proxies^{26,27}. The Materials Project (MP) serves as an ideal platform for novel materials discovery, given the large number of calculated material properties and optimized crystal structures contained in the database²⁸. The database contains 124,515 inorganic compounds with properties calculated via medium / high accuracy DFT methods. The MP team has calculated the elastic tensors for 13,751 and the dielectric tensors for 4,892 inorganic materials so far²⁸ and made these publicly available²⁰. In addition, there are currently 1,974 materials for which MP has calculated both the dielectric and elastic properties. This set of materials is ideal for data mining and training machine learning models to predict electrostrictive response. Starting from

this set, we down-select using a set of simple property filters to find new promising candidates for electrostriction applications. We limit the materials by considering non-elemental (> 1 element) dielectrics with a bandgap > 0.5 eV and seek compounds that should exhibit relative stability as determined via the energy above the hull (< 0.1 eV). The schematic representation of the workflow is shown in Fig. (1).

These materials are then separated into centrosymmetric and non-centrosymmetric datasets based on their point group symmetries. This discretization serves the purpose of allowing us to consider materials lacking an inversion symmetry (non-centrosymmetric), which exhibit a spontaneous polarization via a piezoelectric response resulting from the dielectric and electrostrictive contributions separately from those that solely display an electrostrictive response (see Fig. 1). Taking these latter materials, it is then possible to consider the ratio of (s_R/ϵ^*) for each material and rank these according to the proxies described in Equations (3) and (4). To reduce the dielectric and elastic tensors to a scalar value for each data point, the inverse of the Reuss average bulk modulus was used in place of the elastic compressibility ($s_R \approx 1/K_R$) and the averaged dielectric tensor eigenvalue in place of ϵ^* , thus $Q_h = (K_R \epsilon^*)^{-1}$ is considered a replacement for s/ϵ and a proxy for predicting Q_h . Alternatively, $M_h = (\epsilon^*/K_R)$ is the expression used for querying for high M_h . These proxies are utilized throughout the rest of the study in combination with DFT calculated values for shortlisting materials which should exhibit exceptional electrostrictive strain response to an applied external electric field.

First Principles (DFT) Validation

The accuracy of DFT for materials properties that are determined at the electronic and atomic levels has been well tested; it provides a platform to bridge the gap between fundamental theory, high-throughput computational data science, and experiments^{29–37}. Here, we perform first-principles calculations with DFT using the plane-wave pseudopotential method³⁸. The structural units of the compounds are taken from the MP database. We have used the PBEsol exchange-correlation functional³⁹ in place of the standard General Gradient Approximation (GGA) in the MP. PBEsol is a revised Perdew-Burke-Ernzerhof GGA chosen due to the enhanced prediction of equilibrium properties of densely packed solids, such as the dielectric and elastic tensors for insulating materials compared to GGA²⁵. Geometric optimization was carried out to obtain the equilibrium lattice parameters and corresponding atomic positions. The k-points grid size was set to $9 \times 9 \times 9$, but models with atoms larger than 20 were treated with $7 \times 7 \times 7$ grid size. The kinetic energy cutoff for the plane waves is 800 eV. The symmetry tag was switched on for the calculations so that the system did not deviate from the initialized structures. Non-spin polarized calculations were performed as most compounds were not expected to have a magnetic ground state. Geometrical optimization for the models was carried out with the tolerance for total energy convergence set to 10^{-5} eV and was performed in five cycles. The relaxed model from one cycle was then fed as the initial model for the next cycle to ensure a thorough relaxation. The calculations were performed with the Vienna ab initio simulation package (VASP)^{40–42}.

The elastic compliance tensor was calculated by performing six finite distortions of the supercells and constructing the Hessian matrix from total energies obtained from density functional perturbation theory (DFPT)⁴³. The static ion-clamped dielectric matrix was computed using DFPT via the linear Sternheimer equations^{44,45}. This method bypasses the complexity of

computing the dielectric function through relaxation under finite electric fields. Equations (6) and (7) rely on the change in dielectric response as a function of hydrostatic pressure⁴⁶. The DFT computation of the dielectric function was done at 25 kbar *pstress* above and 25 kbar *pstress* below the equilibrium volume for which the *pstress* is zero. The mechanical perturbation of the order ± 25 kbar is well within the harmonic approximation and provides minimal deviation of the unit cell symmetry. We found slight variations in the equilibrium lattice parameters when compared to the MP. This is due to differences in the pseudopotentials that were utilized in this study in the relaxation procedures.

DISCUSSION

Applying the selection criteria developed in Section III has allowed us to shortlist a set of materials that may potentially exhibit a significant electrostrictive strain response. Q_h^{proxy} values estimated from the MP data using Equations (3) and (4) are compared with the experimental data taken from Refs.^{3-5,47} in Fig. 2. It is observed that specialized polymers have generally larger Q_h than ceramics or glasses. Comparing Q_h of materials from the MP dataset, one finds larger Q_h in several ceramics and covalent salts that surpass polymers by almost 400% if the data from Ref. 3 corresponding to polyurethane elastomer is considered an outlier. The top electrostrictive materials from MP are explored in more detail using more accurate DFT computations. The Q_h^{DFT} values based on Equation (6) display even more promising results with electrostrictive coefficients over 500% larger than typical electrostrictive polymers.

The top ten Q_h (Q_h^{proxy} and Q_h^{DFT}) and M_h (M_h^{proxy} and M_h^{DFT}) candidates from MP and DFT calculations are listed in Tables 1 and 2, respectively. It is encouraging to find that five out

of our top ten high Q_h materials appear in both proxy and DFT data sets. These are: SiCl_4 , BCl_3 , PCl_3 , GaBr_3 , and WCl_6 . On the other hand, three out of the top ten M_h materials appear in both the proxy and DFT data sets. These are SbSI , SbCl_2 , and WCl_6 . Materials in the top ten list of Q_h^{proxy} and M_h^{proxy} include MgCl_2 , MgI_2 , SiCl_4 , WCl_6 , and PCl_3 . Likewise, materials common to the top ten list of Q_h^{DFT} and M_h^{DFT} are WCl_6 , GaBr_3 , and SbCl_3 . Overall, the data supports that the halide groups, especially the chlorides, the bromides, and the iodides are promising materials for electrostriction functionality.

There are important differences in the output value of Q_h that should be noted. For example, our Q_h^{proxy} values for WCl_6 and PBr_3 are $22.83 \text{ m}^4 \text{ C}^{-2}$ and $20.99 \text{ m}^4 \text{ C}^{-2}$, respectively, while Q_h^{DFT} for these compounds is significantly larger: $560.53 \text{ m}^4 \text{ C}^{-2}$ for WCl_6 and $393.32 \text{ m}^4 \text{ C}^{-2}$ for PBr_3 . Other materials such as GaCl_3 have similar values from the empirical and DFT relations ($20.97 \text{ m}^4 \text{ C}^{-2}$ and $17.78 \text{ m}^4 \text{ C}^{-2}$, respectively). We also plot a comparison of Q_h^{proxy} with Q_h^{DFT} and M_h^{proxy} with M_h^{DFT} in Fig. 3(a) and Fig. 3(b), respectively. There are significant deviations from the linear correlation that follows from the Newnham semi-empirical correlation between s_R/ϵ^* and Q_h . The result ascertains that Newnham's semi-empirical relation, Q_h^{proxy} is not a universal measure that is applicable across all materials.

The most striking aspect of the top compounds is that they are halides, chlorides, bromides, and iodides. We anticipated this due to recent observations of high electrostrictive properties in fluorides such as CaF_2 , BaF_2 , SrF_2 , LiF , and NaF with electrostrictive responses around $0.36 - 0.46 \text{ m}^4 \text{ C}^{-2}$ ^{3-5,47}. It is interesting to note that none of these compounds made our top ten obtained either via data mining of MP or from further refinement of MP results through high-precision DFT. The materials that are discovered through our approach are mainly binary non-cubic semi-metal halides. We note that three materials appear common to the top ten Q_h^{DFT}

and top ten M_h^{DFT} datasets: GaBr₃, WCl₆, and SbCl₃. These compounds have not yet been explored with respect to their electrostrictive properties. We certainly hope that our results will generate more experimental work to verify our predictions. We note that not all the compounds in Table 1 are viable materials, some are liquid at room temperature (e.g., SiCl₄, PCl₃, PBr₃O), some are gases or volatile at room pressure (e.g., BCl₃, SF₆, or WCl₆). But others such as GaBr₃ with Q_h^{DFT} of 560.53 m⁴ C⁻² show significant promise.

To explain these results and to identify the origin of the giant electrostrictive properties of materials displayed in Tables 1 and 2, we carried out a detailed analysis of bonding, charge distribution, and hybridization for selected compounds. For example, we have examined GaBr₃, one of the top candidates with $Q_h^{\text{DFT}} = 560.53 \text{ m}^4 \text{ C}^{-2}$ and $M_h^{\text{DFT}} = 2.58 \times 10^{-19} \text{ m}^2 \text{ V}^{-2}$. Its oxide counterpart Ga₂O₃ has significantly lower electrostriction response factor, $Q_h^{\text{DFT}} = 0.02 \text{ m}^4 \text{ C}^{-2}$ and $M_h^{\text{DFT}} = 1.38 \times 10^{-22} \text{ m}^2 \text{ V}^{-2}$. As such, Ga₂O₃ did not make it to our lists even within the top 50 materials. The crystal structure and the atomic charge densities of GaBr₃ and Ga₂O₃ are shown in Fig. 4 (a) and Fig. 4 (b), respectively. The atom resolved density of states (DOS) of the respective materials are plotted in Fig. 4 (c) and Fig. 4 (d). Despite each having 24 electrons per formula units in their valence band, the DOS is quite different. The bandgap observed from the DOS of the two compounds are 3.36 eV for GaBr₃ and 2.04 eV for Ga₂O₃, which is greater than 0.5 eV, a criterion used for our data mining. This corroborates with the charge separation observed between the cation and anion sites shown in Fig. 4 (a) and Fig. 4 (b) for GaBr₃ and Ga₂O₃, respectively. Owing to the large band gaps, the two materials have similar order of magnitude permittivities ($\epsilon_r = 2.86$ for GaBr₃ and $\epsilon_r = 9.28$ for Ga₂O₃). The overall energy spread of both the valence and conduction bands of GaBr₃ is smaller than for Ga₂O₃. In addition,

within these bands, the DOS is composed of narrow peaks for GaBr₃ whereas Ga₂O₃ exhibits a more continuous dispersion of its DOS.

The consequence of DOS differences is fundamentally connected with difference in elastic properties and thus on the compressibility s_R , which for GaBr₃ is 22.67 GPa⁻¹. This value is three orders of magnitude larger than s_R of Ga₂O₃ (0.06 GPa⁻¹). The plot of ϵ_r versus s_R is shown to gain an insight into which physical factors play more important role in the derived properties. Fig. (5) is a four-dimensional plot with ϵ_r and s_R as the abscissa and ordinate. The color coding differentiates the crystal system of the compounds, and the circle diameter scales according to the value of Q_h . Note that the values of s_R and ϵ_r are independently computed using DFT. The figure is divided into four quadrants. Quadrant-II covers the region of large s_R but small ϵ_r , and has large Q_h . Conversely, the quadrant-IV covers the region of small s_R but large ϵ_r , and has smaller Q_h . These seem consistent with the semi-empirical relation of Equation (1). However, we observe that quadrant-III is filled with data points showing that there are several materials with low s_R and low ϵ_r that make up the chemical space. On the other hand, quadrant-I is almost empty. The result does not reflect the same trend as shown in Refs.^{5,10}, indicating that electrostrictive properties cannot be generalized using Newnham's proxy defined through Equations (3) and (4). The ϵ_r and s_R derived from the Materials Project data are shown in Supplementary Figure 1 for all the datamined compounds and is provided in the Supplementary Information.

As a cross-check of the quality of data obtained from our study, we calculated the effective piezoelectric coefficients d and g from the derived Q_h and M_h . The electrostriction coefficients are related to piezoelectric charge (d) and voltage (g) coefficients as:

$$d = 2M_h^{\text{DFT}}F_b \quad (7)$$

$$g = 2 \varepsilon^* Q_h^{\text{DFT}} F_b, \quad (8)$$

where F_b is the breakdown voltage. This quantity essentially determines the maximum amount of strain that can be obtained through an applied electric field which is also true for electrostrictors.

For stress sensing, the piezoelectric charge coefficient (d) relates the applied stress (X_{jk}) to the dielectric displacement generated ($D_i = d_{ijk} \cdot X_{jk}$) in short-circuit conditions whereas the piezoelectric voltage coefficient (g) relates the applied stress to the generated electric field ($E_i = -g_{ijk} \cdot X_{jk}$).

There is no direct way of computing F_b . We used the breakdown voltage expression from Refs. ^{48,49}:

$$F_b = 24.442 \exp\left(0.315 \sqrt{E_g \omega_{\max}}\right) \quad (10)$$

where ω_{\max} is the maximum phonon frequency at the Γ -point that were calculated from the linear response approach and E_g is the DFT obtained band gap. Although the band gap is underestimated in DFT, we do not expect it to affect the results of F_b because Equation (10) is a machine-learned relationship that already accounts for the underestimated band gaps.

Table 3 lists the top ten materials for F_b , d , and g . The magnitudes of d for these materials are smaller than what generally is accepted as promising in the field of linear dielectrics, i.e., few hundreds of 10^{-12} m V⁻¹. The values of g , on the other hand, are three orders of magnitude larger than those commonly appear in linear dielectrics applications. This complements the extremely large effective piezoelectric coefficients obtained on ceria ($d_{33} \sim 2 \times 10^5$ pC N⁻¹), a known ‘giant’ electrostrictor, and underlines the potential of electrostrictors as an alternative to piezoelectrics. As for the top candidates, we find 70% of the materials common in the top ten list of d and g . The data signifies further that fluorides, chlorides,

bromides, and iodides are promising material systems for both linear and quadratic dielectric response.

We have used a data mining backed by first principles calculations approach to down select materials for the discovery of novel electrostrictive materials. Our analysis shows that the halides — fluorides, chlorides, bromides, and iodides, are promising materials systems for high electrostriction response. However, unlike linear dielectrics and ferroelectric glasses, they do not follow Newnham's relation. We note that some of these materials may have significantly larger electrostrictive coefficients (Q_h) than even electroactive polymers. Discovery of electrostrictors with electrostrictive coefficients comparable to the 'giant' electrostrictors, where the physics is governed by active defects, presents the prospect of applications that are limited to low-frequency response as is the case for 'giant' electrostrictors. The corresponding effective piezoelectric voltage coefficients obtained under bias electric field surpass classical piezoelectrics by three orders of magnitude and constitute an appealing alternative to piezoelectrics. We believe that this combination of computational and informatics-based approach will provide the necessary guidance for future experimental work, resulting in a new generation of electrostrictors with exceptionally high property coefficients.

METHODS

The Materials Project database was used for sourcing, compiling, and curating the crystal structure data and the existing elastic compliance and permittivity. The electrostriction coefficient was computed based on Newnham's proxy. It provided early-stage learning for shortlisting a list of compounds for carrying out more detailed first-principles calculations. A set of top candidates was selected for first-principles calculations. A set of randomly selected

compounds was also included in the list. Detailed density functional theory (DFT) calculations using the Vienna *Ab initio* Simulation Package (VASP) were carried out with generalized gradient approximation (GGA) as the exchange-correlation functional and a high-density k-points mesh. The electrostatic coefficient was calculated as a differential of pressure, where DFT calculations were applied with pressure constraint with the *pstress* tag.

DATA AVAILABILITY

The data supporting the results are available upon reasonable request to the authors.

ACKNOWLEDGEMENTS

Authors AG, SKN, and SPA thank the Air Force Research Laboratory, Materials and Manufacturing Directorate (AFRL/RXMS) for support via Contract No. FA8650-18-C-5700. JY and PEJ have been supported by the ANR-19-ASTR-0024-01 and ANR-20-CE08-0012-1 grants.

AUTHOR CONTRIBUTION

The concepts presented herein were conceived by PEJ and SPA. DT performed the data mining process and provided the initial analysis. AG carried out DFT calculations under the supervision of SKN. All authors analyzed the data and prepared the manuscript for publication. DT and AG contributed equally for this work.

COMPETING INTERESTS

The Authors declare no Competing Financial or Non-Financial Interests

REFERENCES

1. Fanson, J. L. & Ealey, M. A. Articulating fold mirror for the Wide-Field/Planetary Camera II. in *Proc.SPIE* vol. 1920 (1993).
2. Uchino, K. Electrostrictive Actuators: Materials and Applications. *Am. Ceram. Soc. Bull.* **65**, 647–652 (1986).
3. Li, F., Jin, L., Xu, Z. & Zhang, S. Electrostrictive effect in ferroelectrics: An alternative approach to improve piezoelectricity. *Appl. Phys. Rev.* **1**, 011103 (2014).
4. Uchino, K., Nomura, S., Cross, L. E., Newnham, R. E. & Jang, S. J. Electrostrictive effect in perovskites and its transducer applications. *J. Mater. Sci.* **16**, 569–578 (1981).
5. Newnham, R. E., Sundar, V., Yimnirun, R., Su, J. & Zhang, Q. M. Electrostriction: Nonlinear electromechanical coupling in solid dielectrics. *J. Phys. Chem. B* **101**, 10141–10150 (1997).
6. Yuan, J. *et al.* Giant Electrostriction of Soft Nanocomposites Based on Liquid Crystalline Graphene. *ACS Nano* **12**, 1688–1695 (2018).
7. Li, Q. *et al.* Giant thermally-enhanced electrostriction and polar surface phase in La₂Mo₂O₉ oxygen ion conductors. *Phys. Rev. Mater.* **2**, 41403 (2018).
8. Korobko, R. *et al.* Giant Electrostriction in Gd-Doped Ceria. *Adv. Mater.* **24**, 5857–5861 (2012).
9. Chen, J., Shurland, A., Perry, J., Ossmann, B. & Gururaja, T. R. Electrostrictive transducers for medical ultrasonic applications. in *ISAF '96. Proceedings of the Tenth IEEE International Symposium on Applications of Ferroelectrics* vol. 1 27–30 (1996).
10. Damjanovic, D. & Newnham, R. E. Electrostrictive and Piezoelectric Materials for Actuator Applications. *J. Intell. Mater. Syst. Struct.* **3**, 190–208 (1992).
11. Pilgrim, S. M. & Revathi, S. B. T.-R. M. in M. S. and M. E. Electrostrictive Ceramics for Sonar Projectors. in (Elsevier, 2016).
12. Anam, M. K., Gopalakrishnan, P., Sebastian, A. & Ahn, E. C. Proposal for an electrostrictive logic device with the epitaxial oxide heterostructure. *Sci. Rep.* **10**, 14636 (2020).
13. Yavo, N. *et al.* Large Nonclassical Electrostriction in (Y, Nb)-Stabilized δ -Bi₂O₃. *Adv. Funct. Mater.* **26**, 1138–1142 (2016).
14. Luna, A. *et al.* Giant Electrostrictive Response and Piezoresistivity of Emulsion Templated Nanocomposites. *Langmuir* **33**, 4528–4536 (2017).
15. Park, D.-S. *et al.* Induced giant piezoelectricity in centrosymmetric oxides. *Science (80-.)*. **375**, 653–657 (2022).
16. Yu, J. & Janolin, P.-E. Defining ‘Giant’ Electrostriction. *J. Appl. Phys.* **131**, 170701 (2022).
17. Chen, B. *et al.* Large electrostrictive response in lead halide perovskites. *Nat. Mater.* **17**, 1020–1026 (2018).
18. Tanaka, I., Rajan, K. & Wolverton, C. Data-centric science for materials innovation. *MRS Bull.* **43**, 659–663 (2018).
19. Suh, C., Fare, C., Warren, J. A. & Pyzer-Knapp, E. O. Evolving the Materials Genome: How

- Machine Learning Is Fueling the Next Generation of Materials Discovery. *Annu. Rev. Mater. Res.* **50**, 1–25 (2020).
20. Toonder, J. M. J. den, Dommelen, J. A. W. van & Baaijens, F. P. T. The relation between single crystal elasticity and the effective elastic behaviour of polycrystalline materials: theory, measurement and computation. *Model. Simul. Mater. Sci. Eng.* **7**, 909–928 (1999).
 21. De Jong, M. *et al.* Charting the complete elastic properties of inorganic crystalline compounds. *Sci. Data* **2**, 1–13 (2015).
 22. Makagon, E. *et al.* All-Solid-State Electro-Chemo-Mechanical Actuator Operating at Room Temperature. *Adv. Funct. Mater.* **31**, 2006712 (2021).
 23. Jiang, Z. *et al.* Electrostriction coefficient of ferroelectric materials from ab initio computation. *AIP Adv.* **6**, 065122 (2016).
 24. Kornev, I., Willatzen, M., Lassen, B. & Lew Yan Voon, L. C. Electrostriction Coefficients of GaN, AlN, MgO and ZnO in the Wurtzite Structure from First- Principles. *AIP Conf. Proc.* **1199**, 71–72 (2010).
 25. Tanner, D. S. P., Bousquet, E. & Janolin, P. E. Optimized Methodology for the Calculation of Electrostriction from First-Principles. *Small* **17**, 2103419 (2021).
 26. Sahoo, T., Anene, U. A., Nayak, S. K. & Alpay, S. P. Electronic and optical properties of zinc based hybrid organic-inorganic compounds. *Mater. Res. Express* **7**, 35701 (2020).
 27. Nayak, S. K. *et al.* Insight into point defects and impurities in titanium from first principles. *npj Comput. Mater.* **4**, 11 (2018).
 28. Jain, A. *et al.* The Materials Project: A materials genome approach to accelerating materials innovation. *APL Mater.* **1**, 11002 (2013).
 29. Trujillo, D., Ghosh, A., Nakhmanson, S. M., Sahoo, S. & Alpay, S. P. Surface structure and energetics of low index facets of bismuth ferrite. *Phys. Chem. Chem. Phys.* **22**, 16400–16406 (2020).
 30. Sahoo, S., Dekel, D. R., Maric, R. & Alpay, S. P. Atomistic Insights into the Hydrogen Oxidation Reaction of Palladium-Ceria Bifunctional Catalysts for Anion-Exchange Membrane Fuel Cells. *ACS Catal.* **11**, 2561–2571 (2021).
 31. Adeagbo, W. A. *et al.* Theoretical investigation of iron incorporation in hexagonal barium titanate. *Phys. Rev. B* **100**, 184108 (2019).
 32. Sahoo, S., Rollmann, G. & Entel, P. Segregation and ordering in binary transition metal clusters. *Phase Transitions* **79**, 693–700 (2006).
 33. Esquinazi, P. D. *et al.* Defect-Induced Magnetism in Nonmagnetic Oxides: Basic Principles, Experimental Evidence, and Possible Devices with ZnO and TiO₂. *Phys. status solidi (b)*. **257**, 1900623 (2020).
 34. Sahoo, S., Alpay, S. P. & Hebert, R. J. Surface phase diagrams of titanium in Oxygen, Nitrogen and Hydrogen environments: A first principles analysis. *Surf. Sci.* **677**, 18–25 (2018).
 35. Nayak, S. K. *et al.* Chromium point defects in hexagonal BaTiO₃: A comparative study of first-principles calculations and experiments. *Phys. Rev. B* **91**, 155105 (2015).
 36. Sahoo, S. *et al.* Magnetic properties of small Pt-capped Fe, Co, and Ni clusters: A density functional theory study. *Phys. Rev. B* **82**, 54418 (2010).
 37. Curry, E. B. *et al.* Optical response of nickel-based superalloy Inconel-718 for applications in

- additive manufacturing. *J. Appl. Phys.* **127**, 245111 (2020).
38. Jones, R. O. & Gunnarsson, O. The density functional formalism, its applications and prospects. *Rev. Mod. Phys.* **61**, 689–746 (1989).
 39. Csonka, G. I. *et al.* Assessing the performance of recent density functionals for bulk solids. *Phys. Rev. B* **79**, 155107 (2009).
 40. Kresse, G. & Furthmüller, J. Efficiency of ab-initio total energy calculations for metals and semiconductors using a plane-wave basis set. *Comput. Mater. Sci.* **6**, 15–50 (1996).
 41. Kresse, G. & Furthmüller, J. Efficient iterative schemes for *ab initio* total-energy calculations using a plane-wave basis set. *Phys. Rev. B* **54**, 11169–11186 (1996).
 42. Kresse, G. & Joubert, D. From ultrasoft pseudopotentials to the projector augmented-wave method. *Phys. Rev. B* **59**, 1758–1775 (1999).
 43. Baroni, S., Giannozzi, P. & Andrea Testa. Green's-function approach to linear response in solids. *Phys. Rev. Lett.* **58**, 1861–1864 (1987).
 44. Gajdoš, M., Hummer, K., Kresse, G., Furthmüller, J. & Bechstedt, F. Linear optical properties in the projector-augmented wave methodology. *Phys. Rev. B* **73**, 45112 (2006).
 45. Baroni, S. & Resta, R. Ab initio calculation of the macroscopic dielectric constant in silicon. *Phys. Rev. B* **33**, 7017–7021 (1986).
 46. Francis, G. P. & Payne, M. C. Finite basis set corrections to total energy pseudopotential calculations. *J. Phys. Condens. Matter* **2**, 4395–4404 (1990).
 47. Uchino, K. & Cross, L. E. Electrostriction and Its Interrelation with Other Anharmonic Properties of Materials. *Jpn. J. Appl. Phys.* **19**, L171–L173 (1980).
 48. Kim, C., Pilania, G. & Ramprasad, R. Machine Learning Assisted Predictions of Intrinsic Dielectric Breakdown Strength of ABX₃ Perovskites. *J. Phys. Chem. C* **120**, 14575–14580 (2016).
 49. Kim, C., Pilania, G. & Ramprasad, R. From Organized High-Throughput Data to Phenomenological Theory using Machine Learning: The Example of Dielectric Breakdown. *Chem. Mater.* **28**, 1304–1311 (2016).
 50. Nye, J. F. *Physical Properties of Crystals: Their Representation by Tensors and Matrices.* (1957).
 51. Lines, M. E. & Glass, A. M. *Principles and Applications of Ferroelectrics and Related Materials.* (1979).
 52. Chaboche, J. L. Unified Cyclic Viscoplastic Constitutive Equations: Development, Capabilities, and Thermodynamic Framework. in *Unified Constitutive Laws of Plastic Deformation* (eds. Krausz, A. S. & Krausz, K.) 1–68 (Academic Press, 1996). doi:<https://doi.org/10.1016/B978-012425970-6/50002-3>.

FIGURE CAPTIONS

Figure 1. Flow chart showing data curating and first-principles computation on data-mined compounds. Data-mining Materials Project database and DFT computation workflow for search of high electrostriction materials.

sgae@centralesupelec.fr **Figure 2. Comparison of Q_h electrostrictive coefficient between different materials class.** Magnitude of Q_h values obtained from experiments (data taken from Ref. ³) and compared to Q_h^{proxy} and Q_h^{DFT} from our study.

Figure 3. Comparison of electrostrictive coefficients of Q_h and of M_h obtained from proxy and DFT computation. Comparison of (a) Q_h^{DFT} versus Q_h^{proxy} and (b) M_h^{DFT} versus Q_h^{proxy} obtained from direct application of empirical formula to the Materials Project data and our DFT computations.

Figure 4. Electronic structure of selected compounds. The crystal structure and the charge densities of GaBr₃ and Ga₂O₃ are shown in (a) and (b). The atom projected electronic density of states for GaBr₃ and Ga₂O₃ are shown in (c) and (d).

Figure 5. Plot of permittivity versus compressibility obtained from DFT calculations. Electrostrictive coefficient Q_h^{DFT} as in Equation (3) falls along the quadrants I and III with larger Q_h^{DFT} values appearing in quadrant-III and small Q_h^{DFT} values in quadrant-I.

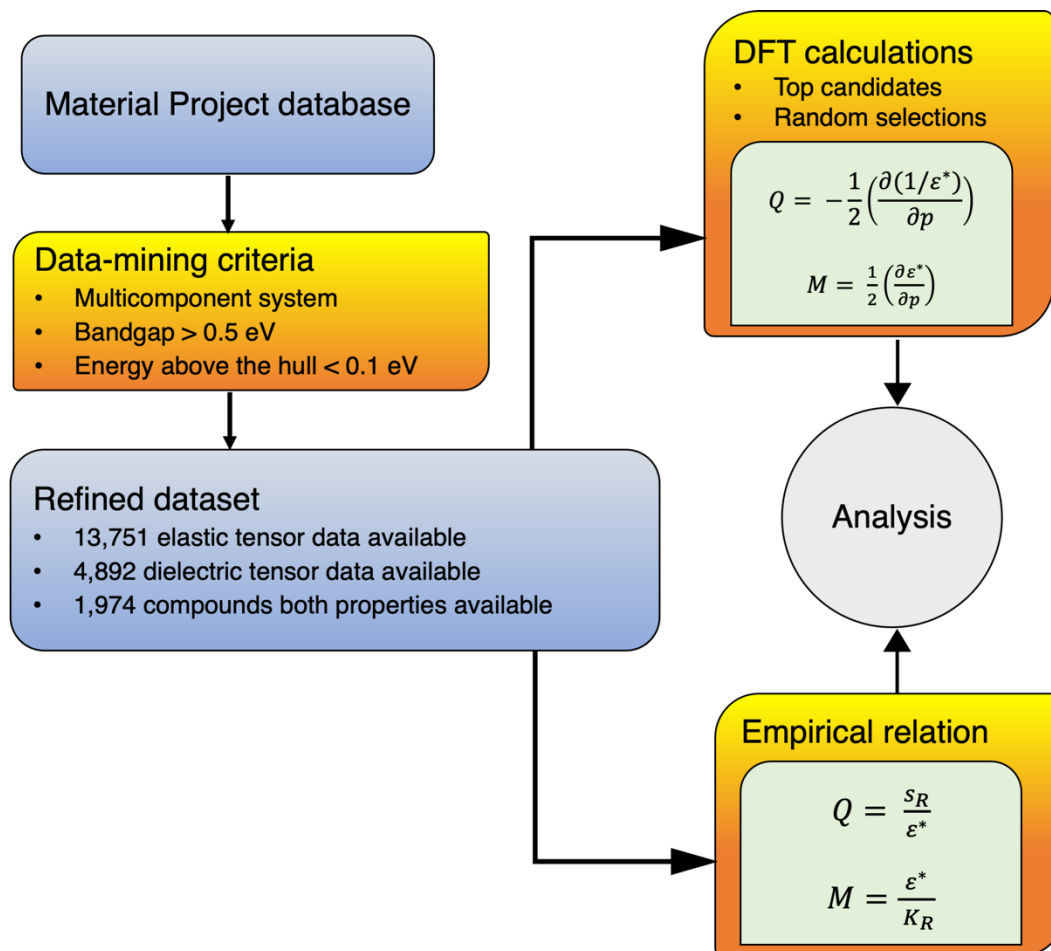


Figure 1.

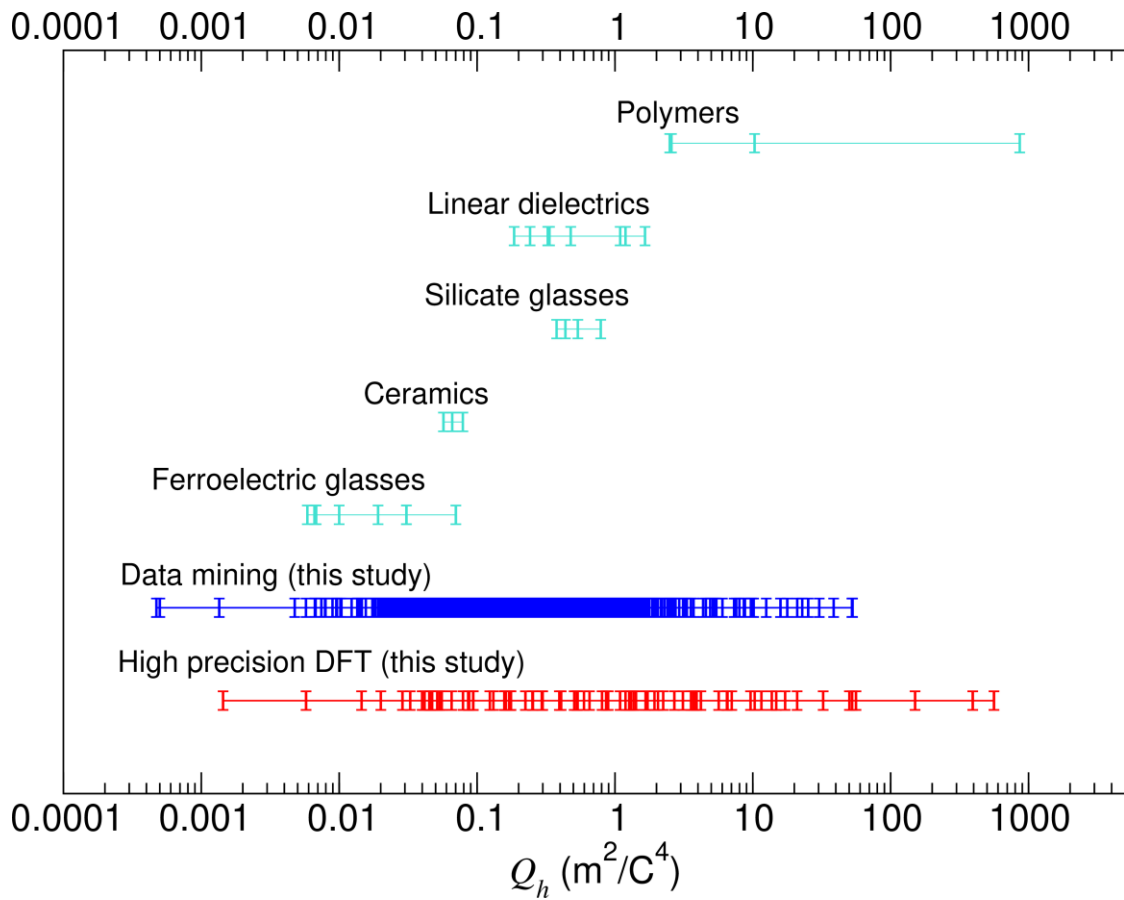


Figure 2.

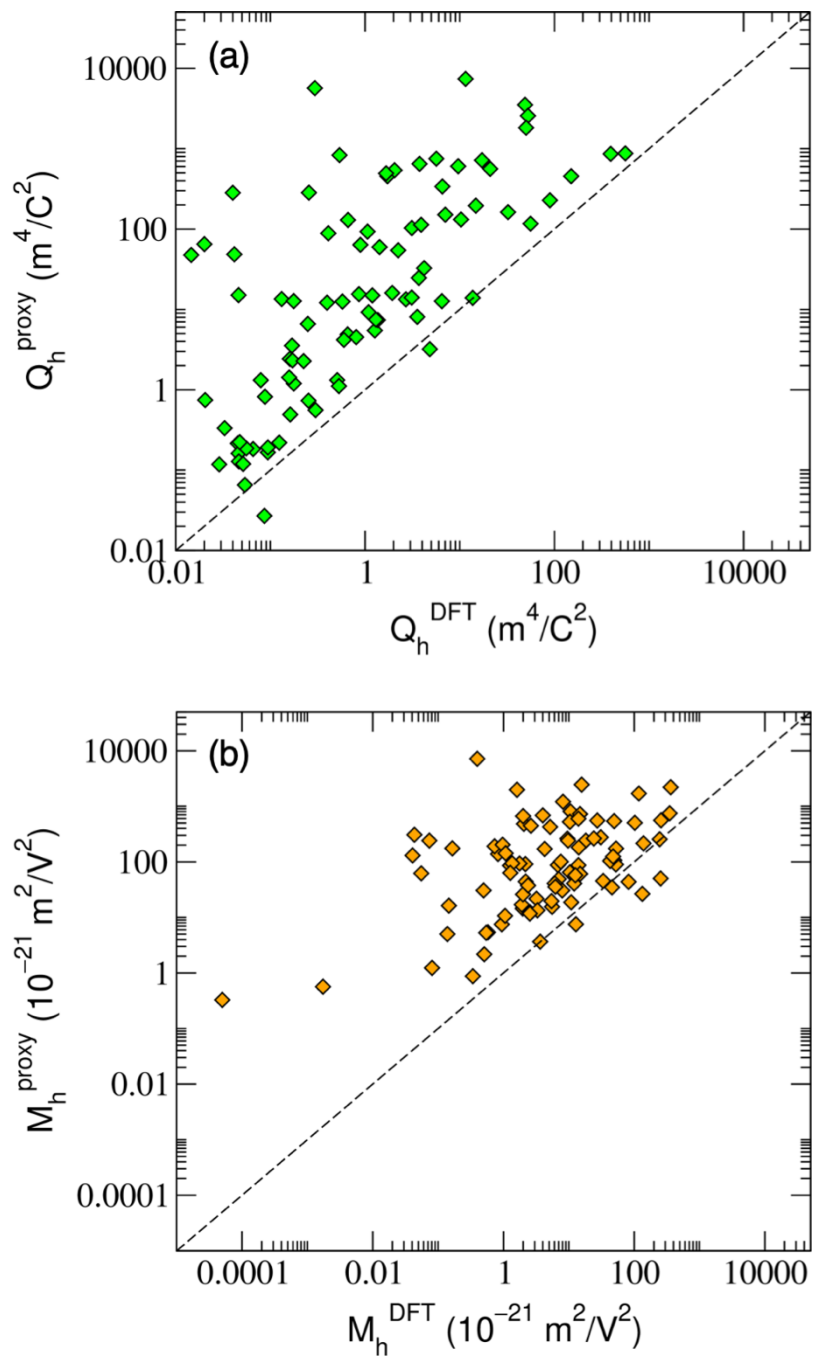


Figure 3.

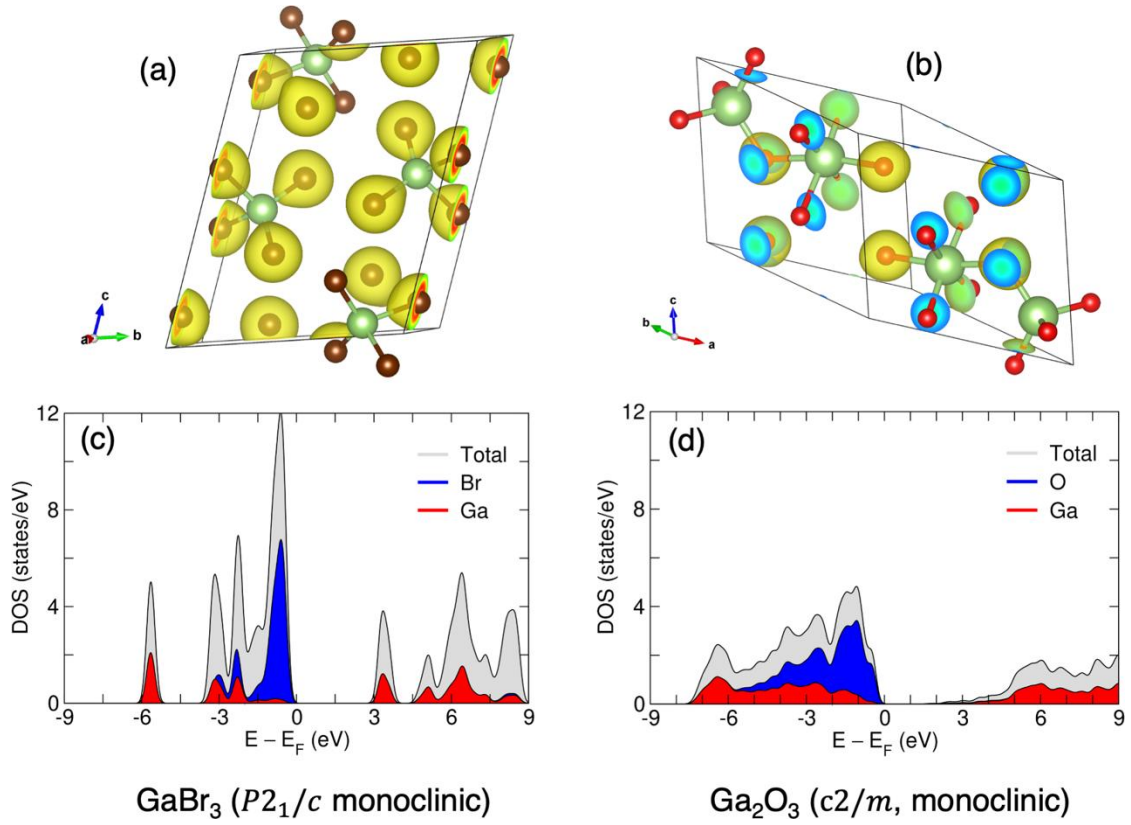


Figure 4.

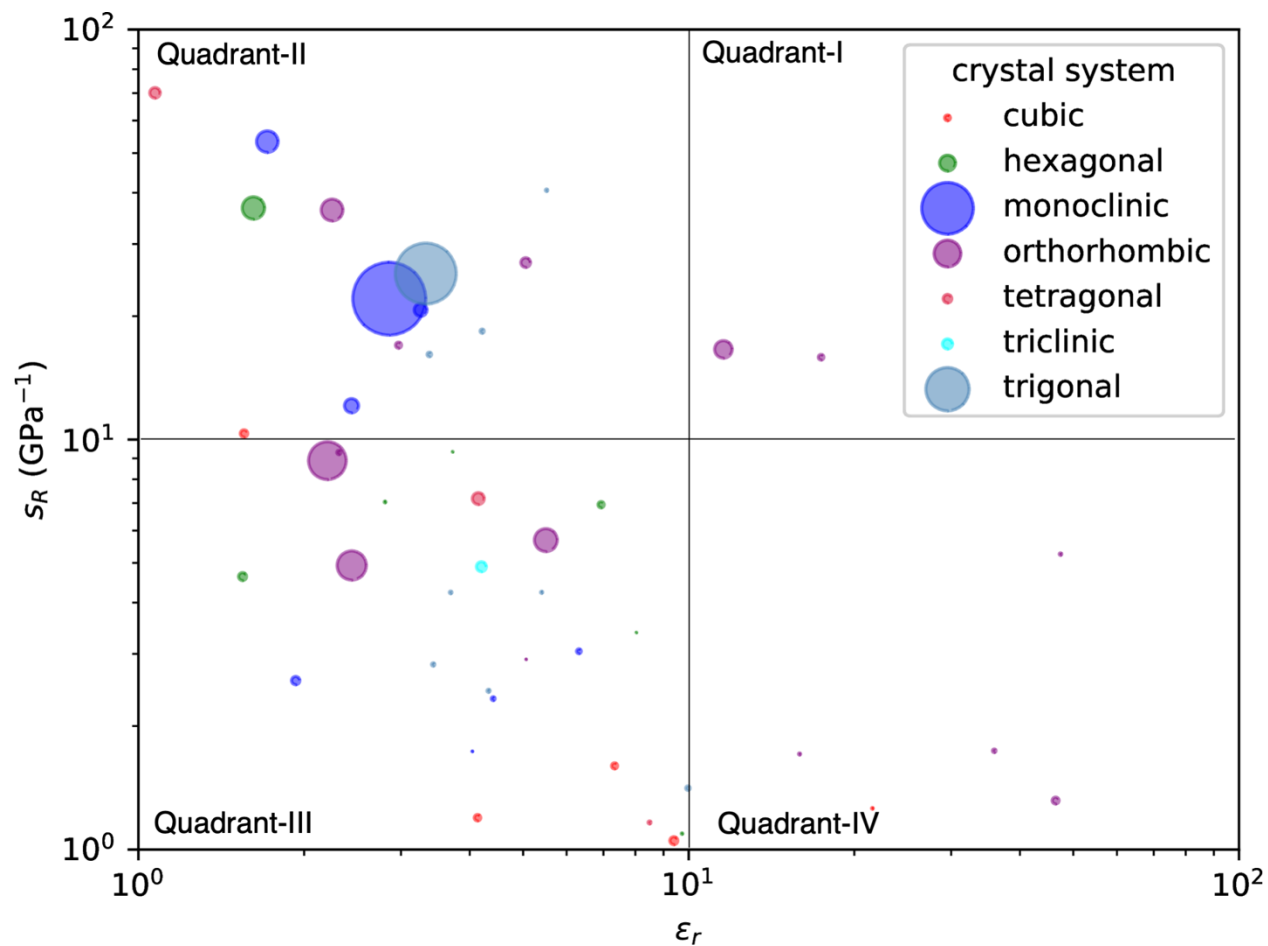


Figure 5.

Table 1. The list of top ten Q_h materials predicted from Newnham's proxy relation (Q_h^{proxy}) and our DFT calculations (Q_h^{DFT}). The unit of Q_h is m^4/C^2 . All calculations were carried out at 0K and therefore on materials in their solid states.

Material	Q_h^{proxy}	Material	Q_h^{DFT}
TeBr ₂	7387.95	GaBr ₃	560.53
MgCl ₂	5666.93	WCl ₆	393.32
SiCl ₄	3512.25	PBr ₃	150.39
BCl ₃	2564.01	PBr ₃ O	89.60
PCl ₃	1824.01	IBr	56.01
GaBr ₃	872.82	BCl ₃	52.49
WCl ₆	862.60	PCl ₃	50.18
MgI ₂	831.07	SiCl ₄	48.97
SF ₆	751.43	SbCl ₃	32.34
AlI ₃	718.53	GaCl ₃	20.97

Table 2. The list of top ten M_h materials predicted from Q_h^{proxy} and our DFT calculations (Q_h^{DFT}). The unit of M_h is $10^{-21} \text{ m}^2/\text{V}^2$. All calculations were carried out at 0K and therefore on materials in their solid states.

Material	M_h^{proxy}	Material	M_h^{DFT}
MgCl ₂	720.364	SbSI	36.375
GaCl ₂	244.796	WCl ₆	35.0125
SbSI	220.457	GaBr ₃	25.797
MgI ₂	198.097	SnBrF	25.429
SbCl ₃	169.936	NaTaN ₂	24.595
Ta(ICl) ₂	120.947	LiBiS ₂	13.865
SiCl ₄	80.925	SnClF	13.275
WCl ₆	74.850	SbCl ₃	11.743
PCl ₃	72.277	Sr ₂ HfO ₄	10.210
CaI ₃	68.584	TePb	8.194

Table 3. Values of dielectric breakdown, F_b , piezoelectric coefficients d , and g computed from calculated from Eq. (7), Eq. (8), and Eq (9), respectively. The unit of F_b , d , and g are MV/m, 10^{-12} m/V and, Vm/N, respectively. The data for of top-ten materials are tabulated. **All calculations were carried out at 0K and therefore on materials in their solid states.**

Material	F_b	Material	d	Material	g
BF ₃	5928.45	GaBr ₃	58.00	Sr ₂ HfO ₄	75.35
PF ₅	1623.23	Sr ₂ HfO ₄	42.19	BiCl ₃	18.83
BN	860.15	WCl ₆	36.09	SbCl ₃	9.49
SF ₆	838.29	PBr ₃ O	34.13	GaBr ₃	9.10
RbAlF ₄	755.88	SbSI	34.06	WCl ₆	3.97
AlClO	678.54	SnBrF	29.85	PBr ₃ O	3.27
BeCl ₂	673.20	SbCl ₃	29.13	BF ₃	2.75
BCl ₃	508.29	BF ₃	25.89	NaTa ₂ N ₂	2.40
Rb ₂ GeF ₆	457.35	NaTa ₂ N ₂	25.91	SnCl ₂	2.34
Cs ₂ NaYF ₆	433.43	SnClF	19.72	GaCl ₂	2.26

Supplementary Information
Data-Driven Methods for Discovery of Novel Electrostrictive Materials

Dennis Trujillo,^{a,b} Ashok Gurung,^c Jiacheng Yu,^d Sanjeev K. Nayak,^a S. Pamir Alpay,^{a,c}
and Pierre-Eymeric Janolin^{d,*}

^a *Department of Materials Science and Engineering and Institute of Materials Science,
University of Connecticut, Storrs, CT 06269, USA*

^b *X-Ray Science Division, Argonne National Laboratory, Lemont, IL 60654, USA*

^c *Department of Physics, University of Connecticut, Storrs, CT 06269, USA*

^d *Universite Paris-Saclay, CentraleSupélec, CNRS, Laboratoire SPMS, 91190, Gif-sur-Yvette,
France*

**email : pierre-eymeric.janolin@centralesupelec.fr*

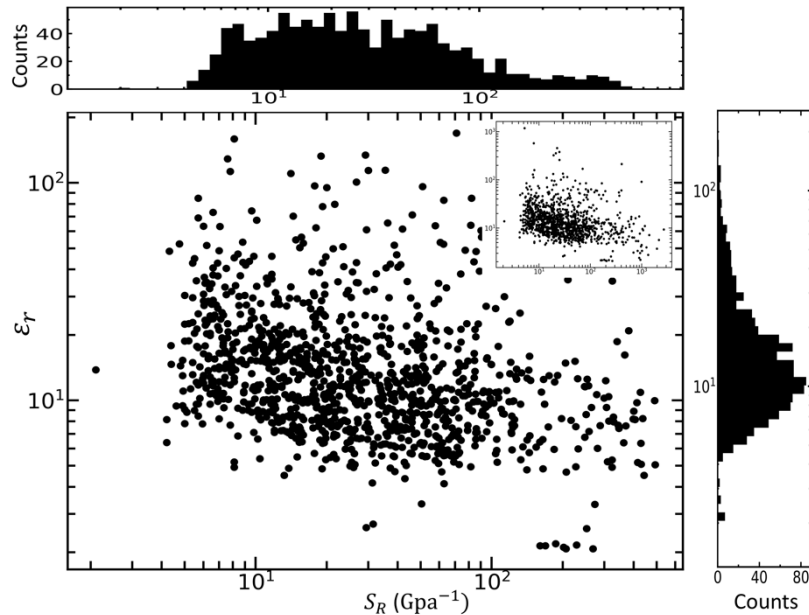


Figure S1 : The scatter plot of ϵ_r and s_R derived from the Materials Project data for the datamined compounds showing nonagreement with Newnham's $s_R \sim \epsilon_r$ linear relationship. The inset shows the data in full scale. The upper and the side graphs show the histogram of number of compounds matching the given value of s_R and ϵ_r , respectively.